Contents lists available at ScienceDirect

Chemical Engineering Research and Design

journal homepage: www.elsevier.com/locate/cherd

Experimental and CFD studies of power consumption in the agitation of highly viscous shear thinning fluids

Marti Cortada-Garcia[a], *Valentina Dore*[b], *Luca Mazzei*[a,*], *Panagiota Angeli*[a,*]

[a] *University College London, United Kingdom*
[b] *GlaxoSmithKline Consumer Healthcare, United Kingdom*

ARTICLE INFO

Article history:
Received 19 July 2016
Received in revised form 21 December 2016
Accepted 13 January 2017
Available online 24 January 2017

Keywords:
Computational fluid dynamics
Non-Newtonian fluids
Rheology oral health products

ABSTRACT

Mixing of non-Newtonian fluids is widely encountered in the process industries. In this research, we obtained a constitutive expression that relates the viscosity of a mixture of glycerol and a gel formed of polyethylene glycol and Carbomer to the shear rate, temperature and mass fraction of one of the two components. We found that the mixtures of these two fluids were well characterized by a non-Newtonian power law model. We then used a number of homogeneous mixtures of the two fluids at different temperatures and mass fractions in a simple stirred tank agitated mechanically by a Rushton turbine to derive experimental power curves, which we then derived numerically in a CFD model by replicating the experimental conditions. We used a combination of an air bearing and a load cell to precisely measure the power required by the impeller to agitate the non-Newtonian mixtures. The computational and experimental results are in good agreement, indicating that the rheological data and the CFD model are accurate.

Introduction

Mechanically stirred vessels are widely used in a broad range of chemical process industries, and their purpose varies from mixing different materials or generating solids suspensions to enhancing heat and mass transfer. The geometric configuration of both impeller and tank, together with the fluid physical properties, in particular viscosity, dramatically affect the fluid dynamics of the system. For Newtonian fluids general guidelines for the most appropriate geometric configuration in different applications are available in the literature (Paul et al., 2004; Zlokarnik, 2003; Nienow et al., 1997). Conversely, even if non-Newtonian fluids are employed in many industrial processes, less information is available about them. These fluids are complex to mix, and often sophisticated impeller designs are required (Kresta et al., 2015; Chhabra and Richardson, 2011). This is the case in the oral health industry, where highly viscous non-Newtonian fluids are used in the production of non-aqueous specialized oral care products, such as non-aqueous toothpastes.

Computational fluid dynamics (CFD) is a powerful tool that yields relevant process information and permits assessing the performance of stirred vessels. The software relies on basic balance equations of fluid mechanics, such as mass, linear momentum and energy balance equations, solved on discretized fluid domains defined by the user. A number of researchers have used CFD to study the behaviour of different types of fluids in mechanically stirred tanks with different types of impellers (Chapple et al., 2002; Shekhar and Jayanti, 2002; Adams and Barigou, 2007; Bulnes-Abundis and Alvarez, 2013; Busciglio et al., 2015; Sun and Sakai, 2016; Ramsay et al., 2016). All the previous studies highlighted the importance of validating the CFD models against experimental data. There are three main methods for validating CFD models: (i) power consumption of impellers, (ii) velocity profiles and (iii) change of properties over time. These are briefly reviewed below for non-Newtonian fluid mixing.

Power consumption is probably the most common approach to validate CFD models of stirred tanks. Computationally, the power con-

* *Corresponding authors.*
E-mail addresses: p.angeli@ucl.ac.uk, l.mazzei@ucl.ac.uk (P. Angeli).
http://dx.doi.org/10.1016/j.cherd.2017.01.018

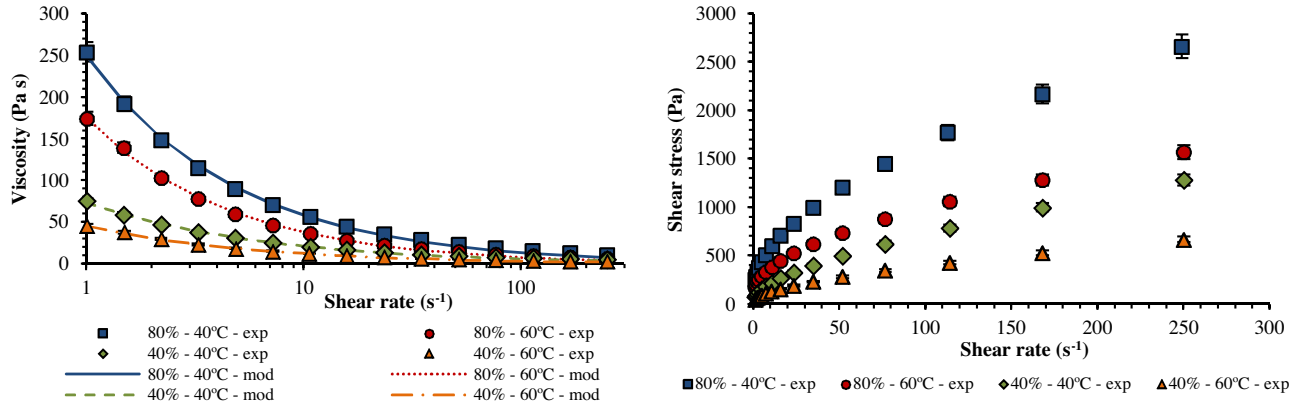

Fig. 1 – Viscosity profile and rheogram of samples at different gel mass fractions and temperatures.

sumption is calculated from the torque applied by the impeller to the fluid:

$$\mathbf{M} = \int_{A_I} \mathbf{r} \times (\boldsymbol{\pi} \cdot \mathbf{n})\, dA \tag{1}$$

where **M** is the overall moment of the stress force about the point located at the bottom of the tank on the axis of rotation of the impeller (the z-axis), **r** is the position vector, **n** is the unit vector normal to the surface, A_I is the surface of the impeller and $\boldsymbol{\pi}$ is the stress tensor, equal to:

$$\boldsymbol{\pi} = pI + \boldsymbol{\tau} \tag{2}$$

where p is the fluid dynamic pressure, I is the identity tensor and $\boldsymbol{\tau}$ is the deviatoric (i.e., the traceless) stress tensor of the fluid.

The power consumption of the impeller can easily be calculated using the following equation:

$$P = 2\pi N M_z \tag{3}$$

where M_z denotes the axial component (that is, the component in the z direction) of the vector **M**, and N is the impeller angular speed in rotations per unit time.

Experimentally, there are a number of different ways to measure the power required for mixing (Ascanio et al., 2004; Paul et al., 2004). In the recent literature on non-Newtonian fluid mixing, investigators have used torque meters extensively to measure power consumption mainly for validating CFD models, as in the following studies. Ameur (2015) studied the efficiency of four impeller configurations (Maxblend, gate, anchor, and double helical ribbon) for mixing yield stress fluids; he used experimental power consumption data available in the literature (Patel et al., 2012) for the anchor and Maxblend impellers to validate the model. Zhang et al. (2014) measured the power during mixing of corn-stover and water (shear thinning fluid) at three different scales (5, 50, and 500 l), and used the findings to validate a CFD model. Pakzad et al. (2013a) studied computationally and experimentally the hydrodynamics and the mixing performance of a coaxial impeller that combined Scaba and anchor geometries for the mixing of yield stress fluids. They developed a correlation for the specific master power curve (power number versus generalised Reynolds number) that applies to the particular system investigated, which they used to validate a CFD model.

Apart from power consumption, velocity fields in the stirred vessel can also be used to validate CFD models. Sossa-Echeverria and Taghipour (2015) obtained velocity profiles of yield stress and shear thinning fluids stirred with three different side-entered axial flow impellers using particle image velocimetry (PIV) and evaluated the cavern formation around the impeller. Comparable results were found with the CFD model. Khapre and Munshi (2015) studied computationally the entropy generated by a Rushton turbine in a baffled tank when mixing shear thinning fluids. The computational velocity profiles were compared against experimental ones available in the literature (Wu and Patterson, 1989; Dyster et al., 1993; Venneker et al., 2010). The previous experimental studies used the Laser-Doppler Anemometry technique (LDA). More information about entropy generation in stirred tanks can be found in Naterer and Adeyinka (2009). Pakzad et al. (2013b) developed a novel and efficient coaxial impeller to agitate yield stress fluids and used CFD to aid the design of the impeller and assess the mixing performance in terms of cavern formation and destruction. The results were validated experimentally with Electrical Resistance Tomography (ERT).

A number of studies have looked at the variation of properties in the mixing system over time as a validating tool for CFD models. Kazemzadeh et al. (2016) studied the mixing time and efficiency of a coaxial mixer (Scaba-anchor system) using yield stress fluids. They developed a CFD model of the mixing system, and they validated experimentally the model using the ERT technique: they injected a tracer in the mixer and they tracked the concentration of it over time at different positions of the vessel. Then, they analysed the effect of the yield stress coefficients together with the speed ratio of the two impellers on the mixing time and power consumption. Hurtado et al. (2015) developed a CFD model of a continuous stirred tank reactor (CSTR), used in wastewater treatment plants, agitated by recirculation of material. To validate the model experimentally, they introduced particles in the system and measured their concentration in the outlet line over time. Patel et al. (2015) developed a CFD model of a baffled stirred tank fitted with a Rushton turbine to quantify the mixing/stagnant volume fraction as a function of the rheological properties of yield stress materials in continuous flow. To evaluate this, a tracer was injected into the inlet and the conductivity of the mixture was measured over time in the outlet. The good agreement between experiments and modelling in the works above demonstrated the applicability of this validation methodology (that is, change of properties over time).

Carbopols are high molecular weight synthetic polymers of acrylic acid that are widely used in the pharmaceuticals and consumer health-

Table 1 – Coefficients of the power law model for different gel mass fractions and temperatures.

Gel mass fraction	Temperature [°C]	K[kg s$^{(n-2)}$ m^{-1}]	n	Mean error [%]
80%	40	249.55	0.3670	8.36
80%	60	175.28	0.3390	7.42
40%	40	73.88	0.4630	5.66
40%	60	45.91	0.4410	6.51

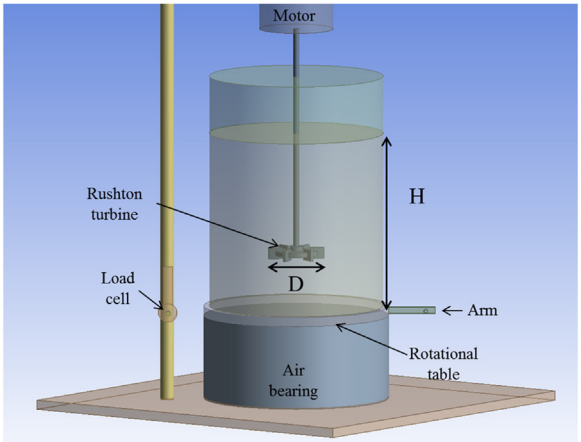

Fig. 2 – Experimental setup.

care industries as thickening agents (Barry and Meyer, 1979). A large number of Carbopol formulations is available. Carbopol gels are usually prepared as dispersions of Carbopol molecules in water, albeit other water-miscible solvents are also used (Bonacucina et al., 2004). The rheological properties of Carbopol gels dramatically depend on the combination of Carbopol molecules and solvent, pH, and temperature. Viscoelasticity is associated to Carbopol gels (Barry and Meyer, 1979; Bonacucina et al., 2004; Coussot et al., 2009). When sufficiently high shear stresses are present, the viscous component dominates over the elastic component, and a number of studies have been presented to derive constitutive expressions to relate the viscosity of Carbopol gels to the shear rate; investigators have modelled Carbopol gels as very highly viscous shear thinning fluids or as Bingham pseudoplastic materials (Islam et al., 2004; Kim et al., 2003; Amanullah et al., 1997; Barry and Meyer, 1979).

In this article, we first aim to characterise the rheology of a non-Newtonian mixture and derive a constitutive equation to model it. The mixture consists of glycerol and a polymer made of polyethylene glycol and Carbopol, which is relevant to the manufacturing of non-aqueous toothpastes. While a lot of information is available in the literature for aqueous Carbomer systems, the rheological behaviour of the combination of glycerol/Carbopol gel has not been studied before. The second objective is to use this rheological information to simulate numerically the fluid dynamic behaviour of the mixture in a stirred vessel and validate the model predictions against accurate experimental results of power consumption obtained in a stirred vessel equipped with a frictionless air bearing and a load cell. This study is part of on-going research that aims to develop a CFD model of a pilot plant mixer used to manufacture non-aqueous toothpastes.

The article is structured as follows. In Section 2, the rheology study of the non-Newtonian mixture and the power consumption measurements in the stirred vessel are presented. The setup of the CFD model is then discussed in Section 3. The computational results on power consumption are finally presented and compared with the experimental findings in Section 4.

2. Experimental setup and methodology

2.1. *Rheology characterization*

The fluids of interest in this research are glycerol and a Carbopol gel made of polyethylene glycol (96%) and Carbomer (4%). The rheological properties of glycerol are available in the literature (Green, 2008), but the rheology of the Carbopol gel has not been studied before. For the development of the CFD model for the mixing of these fluids we need to determine the constitutive equation that describes the viscosity of mixtures of this particular gel with glycerol at different gel mass fractions and shear rates and at different temperatures.

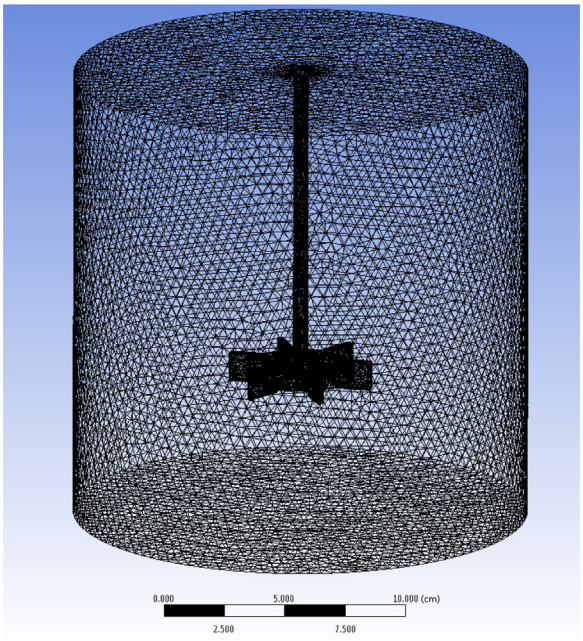

Fig. 3 – Mesh used in the numerical simulations.

We studied the whole range of gel mass fraction in intervals of 10%. This results in 11 mixtures, including the two pure compounds. Each mixture was studied at thirteen equally-spaced temperatures, between 25 °C and 85 °C, this range being dictated by the operating conditions of the industrial mixing process. For each gel concentration and temperature considered, the viscosity of the mixture was evaluated at fifteen equidistant points (in which the experimental results were repeatable) in a logarithmic scale of shear rate in the range of $1\,s^{-1}$– $250\,s^{-1}$. This range is similar to that in other studies (Ramsay et al., 2016; Sossa-Echeverria and Taghipour, 2014; Pakzad et al., 2013b) and is the recommended one for laboratory-scale mixing processes (Schramm, 1994). Moreover, we followed the Metzner–Otto approach (Metzner and Otto, 1957), and we found that the parameter k_s for the impeller is equal to 9.61 ± 1.01, which is in agreement with the literature (Torrez and Andre, 1999). With this k_s value the average shear rates produced by the impeller were found to vary from 8 to $240\,s^{-1}$, which is within the range studied. Viscoelastic properties were checked, and were found not to be significant in the range of our study. Within the shear rate range considered, the error associated with the accuracy of the instrument is negligible. The main source of error of the rheological experiments comes from the heterogeneity in the samples. The rheological experiments were repeated at least twice, and the average standard deviation of all rheology data is 4.55%. The measurements were carried out in an Anton Paar Physica MCR 301 rheometer with parallel plate geometry. In this configuration the shear stress is evaluated at the rim of the upper plate, where both shear stress and shear rate have maximum values. Indicative results are shown in Fig. 1, which correspond to low and high values of gel mass fraction in the mixture (40% and 80%) and to low and high values of temperature (40 °C and 60 °C).

For generalized Newtonian fluids the deviatoric stress tensor $\boldsymbol{\tau}$ is a function of a non-Newtonian (that is, non-constant) viscosity η and of the rate of strain tensor $\boldsymbol{D}$ (equal, by definition, to the symmetric part of the velocity gradient tensor):

$$\boldsymbol{\tau} = -2\eta\boldsymbol{D} \tag{4}$$

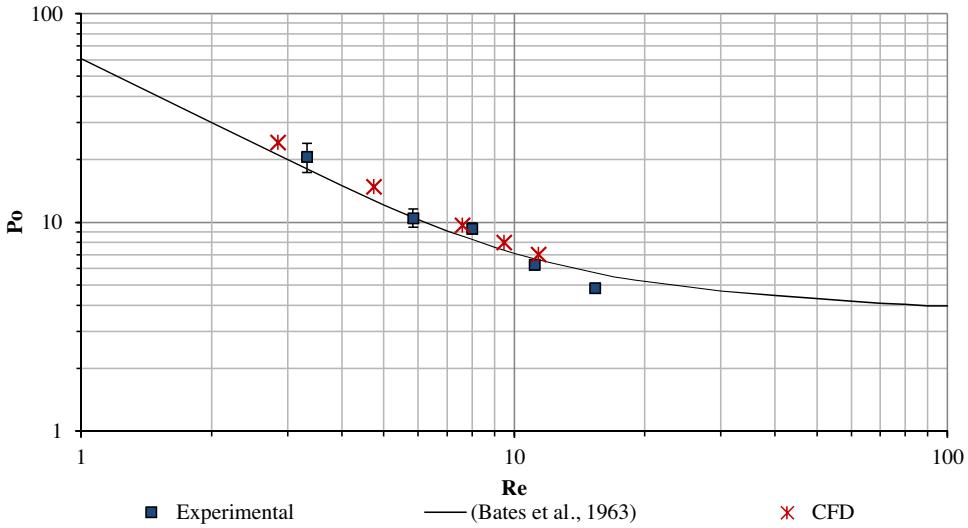

Fig. 4 – Experimental, computational, and bibliographical power curves for Newtonian fluids agitated in an unbaffled tank equipped with a Rushton turbine for geometrically similar systems.

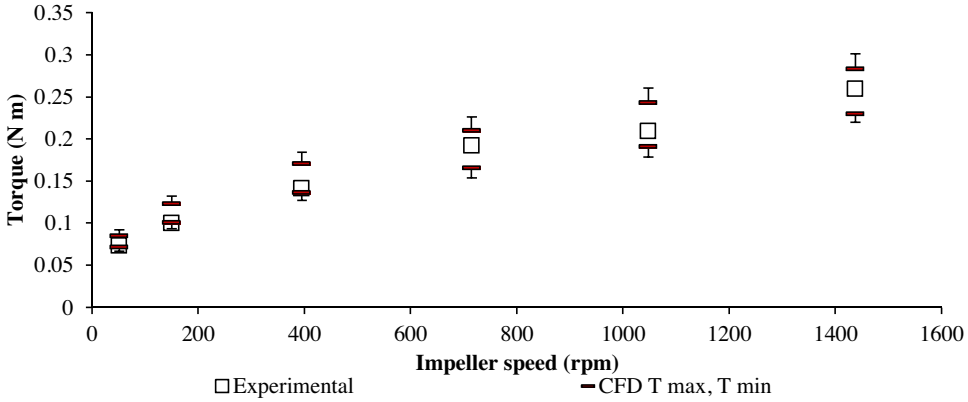

Fig. 5 – Torque vs impeller speed for 80% gel at 60 °C.

The non-Newtonian viscosity η is usually a function of two coefficients: the consistency index K and the power-law index n:

$$\eta = K\dot{\gamma}^{(n-1)} \tag{5}$$

where the shear rate magnitude $\dot{\gamma}$ is a non-negative scalar defined as:

$$\dot{\gamma} \equiv \sqrt{2\,(\boldsymbol{D} : \boldsymbol{D})} \tag{6}$$

Some fluids require a minimum stress to flow, referred to as yield stress (τ_0). If additionally these fluids have shear-thinning behaviour, they can be modelled with the Herschel–Bulkley model:

$$\eta = \begin{cases} \infty, & \tau \le \tau_0 \\ \dfrac{\tau_0}{\dot{\gamma}} + K\dot{\gamma}^{(n-1)}, & \tau \ge \tau_0 \end{cases} \tag{7}$$

where K and n have the same meaning as above, and τ is the magnitude of the deviatoric stress tensor; this is a non-negative scalar defined as:

$$\tau \equiv \sqrt{\frac{1}{2}\,(\boldsymbol{\tau} : \boldsymbol{\tau})} \tag{8}$$

The rheological data obtained were used to fit the parameters K and n of the power law model (to fit the data we used the least-squares method). For the four cases shown in Fig. 1, the values of these parameters are presented in Table 1. This same approach was followed for all conditions studied, and a total of 143 values for each coefficient, K and n, were determined, which correspond to the 11 gel mass fractions and 13 temperatures considered (Appendix A). The coefficients can be calculated at any value of gel mass fraction from 0 to 1 and temperatures from 25 to 85 °C through linear interpolation. The mean interpolation errors for each set of data were calculated using Eq. (9), and are also presented in Table 1.

$$\text{Mean error}\,[\%] = \frac{1}{N}\left[\sum_{i=1}^{N}\frac{|x_{i,\text{exp}} - x_{i,m}|}{x_{i,\text{exp}}}\right] \cdot 100 \tag{9}$$

Here $x_{i,\text{exp}}$ and $x_{i,m}$ are the experimental and modelled values for each set of data, i denotes the number of discrete values and N is equal to 15, which corresponds to the number of shear rate values included in the study for each gel mass fraction and temperature. The mean percentage errors in the estimation of the K and n coefficients for the remaining cases can be found in Appendix A.

The same approach was followed using the Herschel–Bulkley model. We found very good agreement with the experimental data presented in Fig. 1 using both

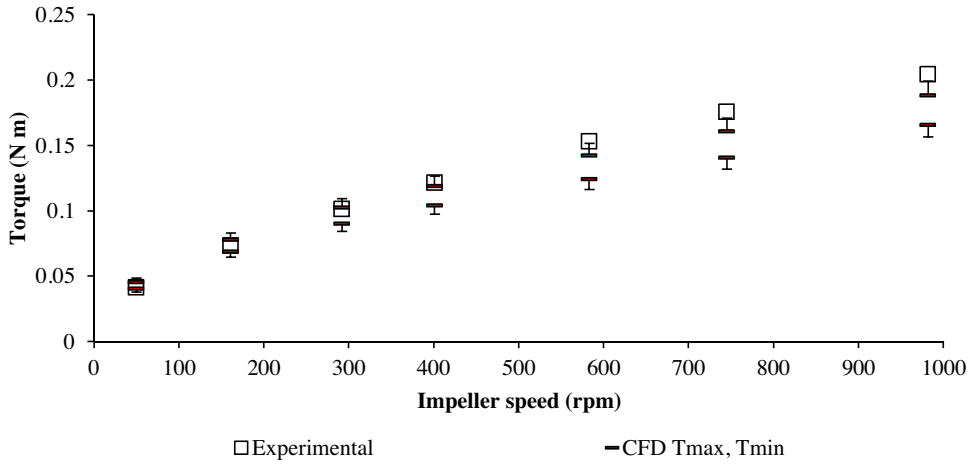

Fig. 6 – Torque vs Impeller speed for 40% gel at 40 °C.

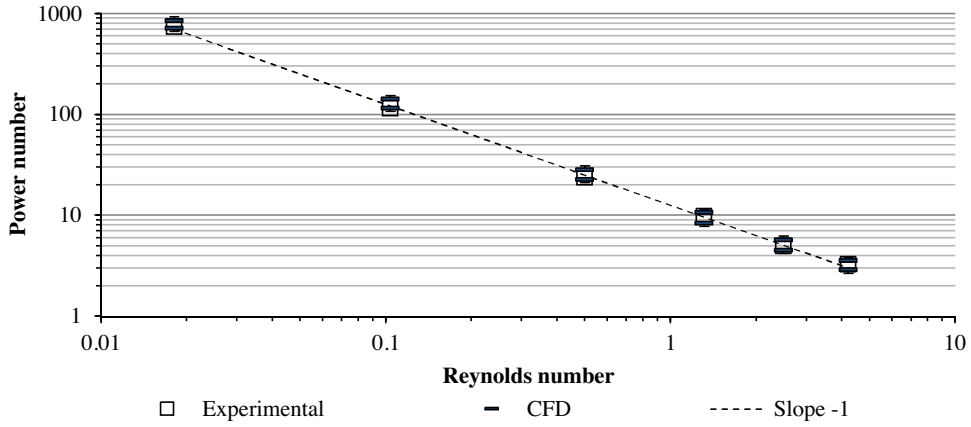

Fig. 7 – Power curve for 80% gel mass fraction and 60 °C.

rheological models; hence, we decided not to present those obtained with the Herschel–Bulkley model in the main article. The list of coefficients of the Herschel–Bulkley model is given in Tables B1, B2, and B3 in Appendix B so they can be used for simulations at different conditions where yield stress may be important.

2.2. *Experimental measurements of power consumption*

Power requirements for the mixing of the Carbomer gel/glycerol solutions were measured experimentally at certain concentrations and temperatures in order to validate the CFD model of the stirred tank with the viscosity function developed from the rheological measurements. The measurements were carried out in a stirred tank fitted with a standard Rushton impeller (Rushton et al., 1950). This configuration was chosen because there are power curves available in the literature for Newtonian fluids, which we used for initial validation of the CFD simulations. The set up consists of a transparent cylindrical tank of internal diameter $D_T = 18.8$ cm and a Rusthon turbine of diameter D = 6 cm. The height of the blades was 1.2 cm. No baffles were present. The height of the fluid, H, was set equal to the tank diameter. The impeller was located at the centre of the tank, 5.4 cm from the bottom, and was driven by a variable-speed motor that could operate in the range of 50–2000 rpm (IKA Eurostar 20) (Fig. 2).

To measure power consumption, torque transducers are often used. These, however, can be inaccurate because they may record the power consumed for mixing the fluid along with losses at the mechanical parts of the rotor. A precise way to measure power consumption is to use an air bearing system (Paul et al., 2004). A schematic of the air bearing system used in this work is shown in Fig. 2. The air bearing is made of metal, has a cylindrical shape and consists of three parts: a main body, an air distribution plate and a rotational table. Air is pumped into the main body via a nozzle at the bottom of the air bearing and reaches the distribution plate at the top. The distribution plate has many holes at its periphery that generate a uniform air layer above it, which lifts the rotational plate. If a stirred tank is placed on top of the rotational plate, the tank is lifted with the plate. When the mechanical stirrer starts rotating, the force transmitted by the impeller to the fluid, and eventually to the tank, makes the tank and the rotational plate rotate at the same angular speed as the impeller. From the force that is required to stop the rotation of the rotational plate, the torque applied by the impeller, and thus the power required to agitate the fluid, can be calculated. This force is measured with a load cell (Omega LCM601-1) and recorded via a data acquisition system and software (Omega IN-USBH). To measure the force, an arm attached to the rotational plate is brought to rest on the load cell as shown in Fig. 2. The power required is calculated using the following equation:

$$P = 2\pi NFx \tag{10}$$

where P (W) is the power required to drive the impeller, N (rev s^{-1}) is the impeller speed, F (N) is the force measured by

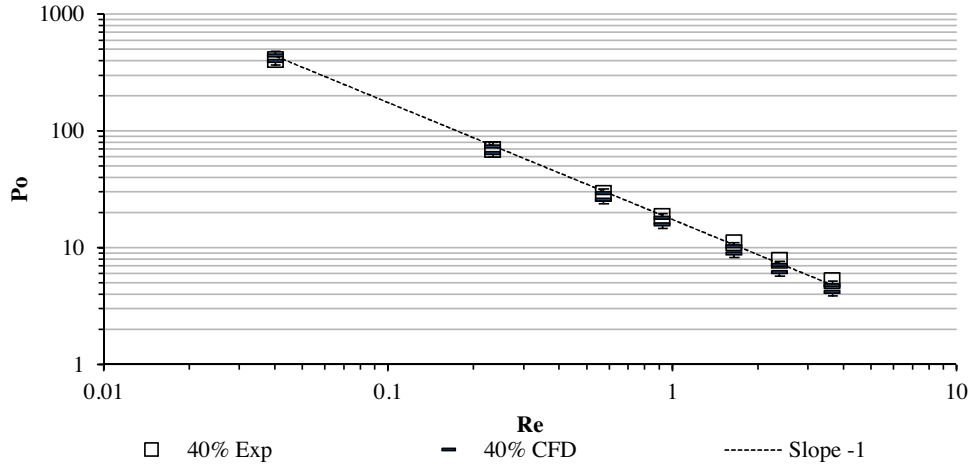

Fig. 8 – Power curve for 40% gel mass fraction and 40 °C.

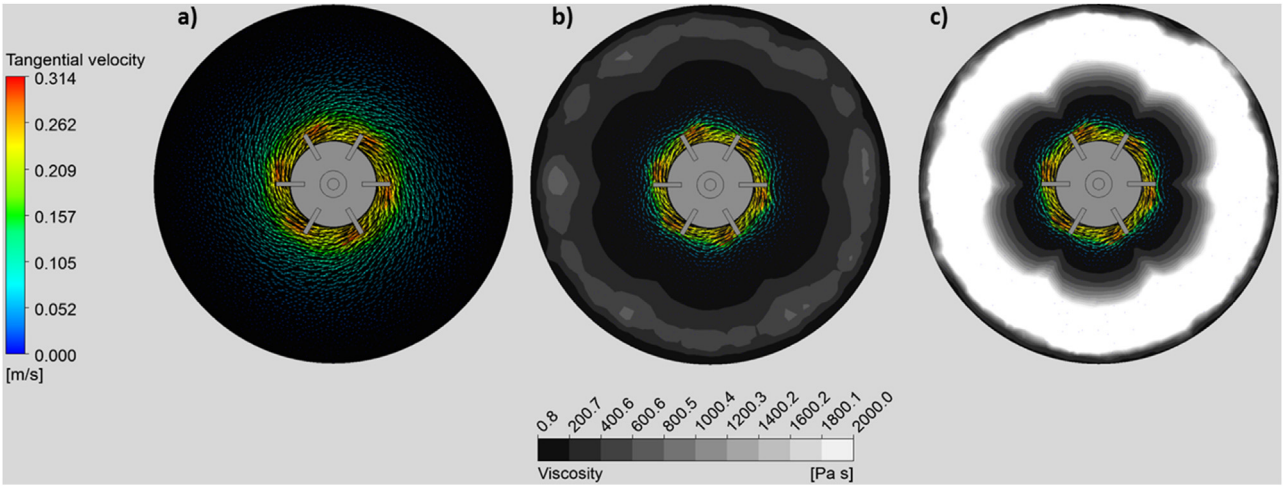

Fig. 9 – Viscosity contours and velocity vectors for (a) glycerol at 20 °C, (b) 80% gel at 60 °C, and (c) 40% gel at 40 °C at 100 rpm.

Table 2 – Comparison among the three mesh qualities studied for the different modelling approaches using the geometry in Fig. 2, with glycerol at 27 °C as working fluid and an impeller speed of 100 rpm.

Mesh quality [#cells]	Approach	Torque impeller [N m]	Time	Error with respect to SM high quality [%]
36,608	RF	$2.91\ 10^{-3}$	80 s	18%
54,067	RF	$2.84\ 10^{-3}$	150 s	20%
156,546	RF	$3.08\ 10^{-3}$	600 s	13%
360,371	RF	$3.49\ 10^{-3}$	25 min	1%
462,558	RF	$3.49\ 10^{-3}$	40 min	1%
31,233	SM	$3.01\ 10^{-3} \pm 5\ 10^{-6}$	100 min	15%
55,442	SM	$3.01\ 10^{-3} \pm 5\ 10^{-6}$	5 h	15%
151,164	SM	$3.16\ 10^{-3} \pm 3\ 10^{-6}$	9 h	11%
361,466	SM	$3.54\ 10^{-3} \pm 3\ 10^{-7}$	24 h	0%
527,832	SM	$3.54\ 10^{-3} \pm 3\ 10^{-7}$	36 h	0%

the load cell, and x (m) is the radial distance from the axis of rotation of the impeller to the application point of the force F (at the centre of the measuring surface of the load cell).

Dimensional analysis of the agitation of non-Newtonian fluids following the power law model shows that the relevant dimensionless groups are the following (Rieger and Novak, 1973):

$$Re \equiv \frac{N^{2\,1-n} D^2 \rho}{K}\ ,\ Po \equiv \frac{P}{N^3 D^5 \rho}\ ,\ n \tag{11}$$

where ρ (kg m^{-3}) is the density of the fluid, D (m) is the diameter of the impeller and n is the power-law index as described above. The first term in Eq. (11) is the Reynolds number Re and the second is the Power number Po. Here we are not accounting for variations of the liquid free surface, generally characterised by the Froude number; this is because the free surface of the high-viscosity fluids considered in this work is essentially always flat at all the conditions investigated.

In the laminar regime, the three dimensionless numbers reported above are related as follows (Rieger and Novak, 1973; Metzner and Otto, 1957):

$$Po = \frac{C(n)}{Re} \text{ with } C(n) = Ak^{n-1} \tag{12}$$

where A and k are constants that depend on the geometry of the impeller and of the tank.

As mentioned, to validate the CFD simulations and provide a baseline for the non-Newtonian case, we studied initially a Newtonian fluid system. For these experiments glycerol at 20 °C was used and stirring was carried out at five impeller speeds (between 1 rpm and 250 rpm) within the laminar flow regime. We investigated only laminar flow because the non-Newtonian fluid mixtures included in the study are highly viscous and at the impeller speeds of interest the flow is laminar. The power measurements with the non-Newtonian mixtures were carried out for two temperatures, 40 °C and 60 °C, gel mass fractions of 100%–20% in intervals of 20% and a minimum of five impeller speeds. The tank containing the sample was put in an oven with temperature control, and was left overnight to let the sample reach the required temperature. The experiments at high temperature were conducted the following day. Prior to the experiments, we measured the temperature at different points in the tank (a minimum of five), and in all cases we found that the maximum temperature difference in space was lower than 5 °C. Once an experiment at high temperature was finished, we left the sample to cool down at room temperature until it reached the required lower temperature. The sample was agitated with the mechanical stirrer described in the paper. When the temperature reached the required value, we again measured it at five different locations and found that the maximum temperature difference was about 5 °C. In all measurements the tank was filled with the fluid, glycerol or gel/glycerol mixture, up to height H, the pressurised air was introduced in the air bearing and for each impeller speed the force required to stop the rotation of the rotating plate of the air bearing was measured with the load cell.

3. CFD solution

3.1. CFD approach

In all our experiments the free surface of the fluid remained flat, even though there were no baffles present. Therefore, to avoid using multiphase models, we simulated only the region occupied by the fluid (so, the computational domain only included this region), which extends from the bottom of the tank up to a height equal to H (Fig. 2). At the top boundary, where the liquid-gas interface is, the three components of the viscous stress force referring to the unit vector normal to the interface were set equal to zero. Additionally, on all the solid surfaces bounding the computational domain, the no-slip boundary condition was applied.

The two main approaches for modelling stirred tanks are the Reference Frame (RF) and the Sliding Mesh (SM). The RF convergences fast, but it is suitable only for steady-state flows. In a stationary frame of reference (stationary relative to the laboratory) the flow in the stirred tank is unsteady. However, the flow is steady relative to a reference frame integral with the impeller, which therefore rotates with a rotational velocity—Ω relative to the stationary frame. This is a non-inertial frame, but the flow is stationary with respect to it. In contrast, SM is suitable also for unsteady flows, for which it provides a time dependent solution, but at the expense of significant computational effort and time. In the SM approach, the geometry should have at least two connected non-deforming sections that slide in relation to each other. All the moving parts (in this case, the impeller) need to be part of the moving zone. For the present studies, we employed as moving zone a cylinder concentric with the impeller, with 10 cm diameter, bottom at 3 cm below the impeller and top at the liquid surface. The elements outside this cylinder formed the stationary zone. In this case it is not necessary to introduce a non-inertial reference frame; instead, the rotational speed (−Ω) can be assigned directly to the moving objects.

RF is the preferred approach when its predictions are the same as those given by the SM approach. To decide what approach to adopt, we tested both of them in two case studies where glycerol at 27 °C and gel at 85 °C were stirred at 100 and 1000 rpm impeller speeds respectively. At these conditions the flow is laminar in both cases. The results of the test are presented in Section 4.

3.2. Rheology implementation

3.2.1. Power law model

We implemented the rheology model via a user defined function to be able to account for the errors presented in Table 1. The coefficients K and n of the power law expression for the fluid viscosity were determined from the experimental rheology curves. Eqs. (4)–(6) were included in the user defined function, and the rate of strain tensor was computed using the partial derivatives of the components of the velocity vector field:

$$\mathbf{D} = \begin{bmatrix} \frac{\partial v_x}{\partial x} & \frac{1}{2}\left(\frac{\partial v_x}{\partial y} + \frac{\partial v_y}{\partial x}\right) & \frac{1}{2}\left(\frac{\partial v_x}{\partial z} + \frac{\partial v_z}{\partial x}\right) \\ \frac{1}{2}\left(\frac{\partial v_x}{\partial y} + \frac{\partial v_y}{\partial x}\right) & \frac{\partial v_y}{\partial y} & \frac{1}{2}\left(\frac{\partial v_z}{\partial y} + \frac{\partial v_y}{\partial z}\right) \\ \frac{1}{2}\left(\frac{\partial v_x}{\partial z} + \frac{\partial v_z}{\partial x}\right) & \frac{1}{2}\left(\frac{\partial v_z}{\partial y} + \frac{\partial v_y}{\partial z}\right) & \frac{\partial v_z}{\partial z} \end{bmatrix} \quad (13)$$

For incompressible fluids, the trace of this tensor vanishes, so that the stress tensor $\boldsymbol{\tau}$ is deviatoric, as previously pointed out.

3.2.2. Herschel–Bulkley model

Some simulations were repeated with the Herschel–Bulkley model to check any differences between the two rheological models. For these cases we used the model embedded in ANSYS Fluent in its default formulation.

3.3. Grid independence

The computational solution depends not only on the modelling approach but also on the grid used in the simulation. Very fine grids give more accurate solutions but are computationally demanding. We aimed therefore to find an optimum grid size that provides a reliable and grid-independent solution at a reasonable time for all the fluids considered in this study. To determine the optimal grid size for the geometry described in Fig. 2, we simulated the agitation of glycerol (Newtonian case) at 27 °C at 100 rpm impeller speed (this results in laminar flow; the Reynolds number is approximately equal to 9.5). Moreover, to ensure that the mesh is also optimum for the non-Newtonian case, we included in this evaluation the fluid with the highest shear thinning behaviour (that of the pure gel at 85 °C), choosing an impeller speed of 1000 rpm, whose corresponding Reynolds number is approximately equal to 5. We used the mesh quality that provided accurate solutions for both extremes. Grid independence was checked for both the

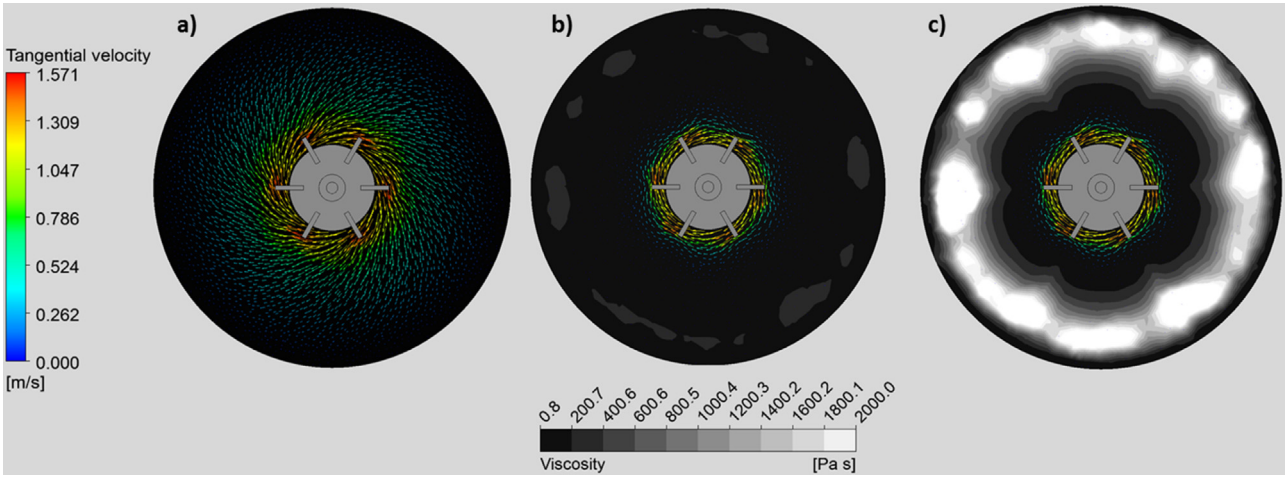

Fig. 10 – Viscosity contours and velocity vectors for (a) glycerol at 20 °C, (b) 80% gel at 60 °C, and (c) 40% gel at 40 °C at 500 rpm.

Table 3 – Comparison among the three mesh qualities studied for the different modelling approaches using the geometry in Fig. 2, with pure gel at 85 °C as working fluid and an impeller speed of 1000 rpm.

Mesh quality [#cells]	Approach	Torque impeller (N m)	Time	Error with respect to SM high quality [%]
36,608	RF	0.114	80 s	4%
54,067	RF	0.116	150 s	3%
156,546	RF	0.115	600 s	3%
360,371	RF	0.117	25 min	2%
462,558	RF	0.117	40 min	2%
31,233	SM	$0.119 \pm 1.4\ 10^{-4}$	100 min	0%
55,442	SM	$0.129 \pm 1.7\ 10^{-4}$	5 h	8%
151,164	SM	$0.121 \pm 2.1\ 10^{-4}$	9 h	1%
361,466	SM	$0.119 \pm 5.5\ 10^{-5}$	24 h	0%
527,832	SM	$0.119 \pm 2.8\ 10^{-5}$	36 h	0%

Reference Frame and the Sliding Mesh modelling approaches (Tables 2 and 3). The SM approach with the highest mesh quality provides the most accurate torque results. Therefore, the difference from this value of the torque computed on the surface of the impeller for each case (Eq. (14)) is also reported in Tables 2 and 3.

$$\text{Error with respect to high quality SM [\%]} = \frac{|M_{impeller,SM,hq} - M_{impeller}|}{M_{impeller,SM,hq}} \cdot 100 \quad (14)$$

For the SM simulations we used a time step equivalent to 1° per step, which allows capturing the transient behaviour of the torque. The simulation was run until a periodic solution was reached, after four complete revolutions. The results presented in Tables 2 and 3 were obtained by averaging the torque on the impeller during the fifth revolution.

The results in Tables 2 and 3 indicate that the RF model provides an accurate solution, particularly when the mesh quality is high for the Newtonian case (fourth and fifth rows of Table 2) and in all mesh qualities studied for the non-Newtonian case (power law model). Moreover, the time required to solve this model is significantly lower compared to the SM approach (e.g. 25 min compared to 24 h for mesh quality about 360k cells). An additional way to evaluate the two approaches is to compare the torque on the surface of the impeller ($M_{impeller}$) against that on the walls of the tank (M_{walls}); by conservation of angular momentum, at steady state the two values of the torque have to be the same. Tables 4 and 5 present the torque computed on the surface of the impeller (Eq. (1)) and the torque difference (as in Eq. (15)) for the different grid sizes and modelling approaches studied.

Table 4 – Comparison between the torques computed on the surface of the impeller and on the walls of the tank for the RF calculations using the geometry in Fig. 2, with glycerol at 27 °C as working fluid and an impeller speed of 100 rpm.

Quality [#cells]	Torque impeller [N m]	Difference in torques [%]
36,608	$2.91\ 10^{-3}$	26%
54,067	$2.84\ 10^{-3}$	36%
156,546	$3.08\ 10^{-3}$	25%
360,371	$3.49\ 10^{-3}$	13%
462,558	$3.49\ 10^{-3}$	3%

Table 5 – Comparison between the torques computed on the surface of the impeller and on the walls of the tank for the RF calculations using the geometry in Fig. 2, with pure gel at 85 °C as working fluid and an impeller speed of 1000 rpm.

Quality [#cells]	Torque impeller (N m)	Error torques
36,608	0.114	4%
54,067	0.116	4%
156,546	0.115	4%
360,371	0.117	4%
462,558	0.117	4%

$$\text{Torque difference [\%]} = \frac{|M_{impeller} - M_{walls}|}{M_{impeller}} \cdot 100 \quad (15)$$

The torque on the walls (M_{walls}) is calculated as the axial component of **M** in Eq. (16):

$$\mathbf{M} = \int_{A_W} \mathbf{r} \times (\boldsymbol{\pi} \cdot \mathbf{n})\, dA \tag{16}$$

where A_W is the surface of the tank walls including the tank bottom.

As we see, the difference in the torque is significant in the first four rows of Table 4, and it is only with the highest quality mesh that a good agreement is obtained. In the case of the non-Newtonian fluid, this error does not depend on the mesh quality, and it is comparable to that of the highest quality mesh for the Newtonian case. We conclude that the optimal mesh quality for our particular model corresponds to the fifth row of Table 4. The mesh is presented in Fig. 3. The computations were carried out using a 3.50 GHz Intel® Xeon® CPU E5-1650 v2 with 16.0 GB RAM. The tank and impeller were drawn with AutoCAD. The different meshes were created with ANSYS Workbench. Unstructured meshes were preferred because of the shape of the impeller. The fluid dynamics were modelled using ANSYS Fluent 16.1. We set up the solution method as follows: for pressure and velocity coupling we used the Coupled strategy; in terms of spatial discretization we used the least squares scheme for evaluating the spatial derivatives, the second order interpolation scheme for the pressure, and the second order upwind scheme for the momentum. For the steady-state simulations, we let the solver run until a plateau was observed on the scaled residuals of the continuity equation, and of the x-, y- and z- velocities. The absolute scaled residuals were recorded and then used as a convergence criterion for the transient simulations.

4. Results and discussion

4.1. Newtonian case

As was discussed before, a few experiments and CFD simulations were carried out with a Newtonian fluid to provide a baseline for the non-Newtonian study. The power number obtained experimentally for the stirring of pure glycerol at 20 °C is plotted against the Reynolds number in Fig. 4. The error bars account for the measurement error of the load cell, which is 0.03% of the maximum value it can read (9.8 N). The results are in good agreement with the power curve suggested in the literature for mixing in geometrically similar systems equipped with a Rushton turbine (the error is less than 10%). In the same figure the power numbers computed with CFD using pure glycerol at 20 °C as working fluid rotating at different impeller speeds from 30 to 120 rpm, RF as modelling approach and highest mesh quality (Table 4) are also shown. As we can see, there is very good agreement between the experimental, computational and bibliographical sets of data.

4.2. Non-Newtonian case

As discussed in Section 2, the torque and power consumption were measured for the mixing of five non-Newtonian glycerol/gel mixtures at a minimum of five impeller speeds and at two different temperatures. In Figs. 5 and 6 the experimental torque values are plotted against the impeller speed for two different cases: 80% gel mass fraction at 60 °C and 40% gel mass fraction at 40 °C. Similar curves were obtained for all the other cases investigated. The errors in these experiments owing to the measuring error of the load cell (0.03% of the maximum value) are negligible, and are not shown. In the same figures, the CFD predictions are also included. We used both the power law and the Herschel–Bulkley models, and minor discrepancies between them were found (less than 1%). We attribute this agreement to the low value of the yield stress compared to the averaged stresses around the impeller computed using the Metzner–Otto approach. Therefore, in what follows we use the power law model.

The stirred vessel was not insulated and there were small variations in the temperature of the mixture during the experiments, both in space and time. To account for this, we measured the temperature at different points inside the mixing tank before and after the torque readings and we used the overall maximum and minimum temperature values recorded for the CFD simulations. Hence, we present two computational results for each experimental measurement, corresponding to the highest and the lowest temperatures recorded. The computational results are also subject to uncertainty that arises from the fitting of the rheological curves when determining the coefficients of the power law model at the different concentrations and temperatures. This error, which is presented in Table 1, was included in the viscosity function and implemented in CFD (Eq. (17)) to determine the error bars of the computational results.

$$\eta = \left(1 \pm \frac{\text{Error}}{100}\right) K\dot{\gamma}^{n-1} \tag{17}$$

At higher temperatures the value of the viscosity is smaller, and consequently the torque is smaller as well. To calculate the lowest values of the torque expected as a result of the fitting error in the simulations with the maximum fluid temperature, we used the negative sign in Eq. (17). Similarly, the lowest temperature would give the highest torque values. In this case, to calculate the highest torque values expected, we used the positive sign in Eq. (17). We used these two extreme cases to determine the computational errors, which decrease the torque values at the high temperature simulations and increase them at the low temperature simulations. We expect the experimental torque to fall between the computational results.

In Fig. 5, all the experimental results fall between the two computational curves. The same happens in Fig. 6 for impeller speeds below 400 rpm. However, at higher impeller speeds the experimental torque values are closer to the upper CFD curve, which corresponds to the minimum experimental temperature. This difference may be caused by the actual temperature distribution inside the tank. We only measured the temperature at a few locations at the beginning and at the end of the experiment, and did not have the complete temperature distribution in space and time. It is possible that most of the fluid in the tank was at low temperature and for this reason the simulated torque values for low temperatures are closer to the experimental ones.

The power curves of the above systems are shown in Figs. 7 and 8, where the Power and Reynolds numbers were calculated from Eq. (11). The experimental error bars are negligible and have been omitted, while the error bars for the CFD simulations are shown, but are very small. As can be seen, the agreement between the computational and experimental data is very good, which indicates that the CFD model can be used to predict the torque applied by a Rushton turbine using the experimental rheology model. In addition, the slope of the

experimental and computational results is very close to −1, which confirms that the flow regime is laminar in all cases. Similar results are found for the other cases considered.

In addition we present the viscosity profiles and velocity vectors of the three different fluids presented above: pure glycerol at 20 °C, gel 80% at 60 °C, and gel 40% at 40 °C agitated at 100 rpm (Fig. 9) and at 500 rpm (Fig. 10) on the plane that corresponds to the middle of the impeller. It is possible to see that the tangential velocity next to the impeller is identical for all fluids on each figure, but the velocity vectors decay very fast in both non-Newtonian fluids compared to the Newtonian case. It can also be observed that the viscosity profiles in the non-Newtonian fluids are heterogeneous due to the shear thinning behaviour: an increase of viscosity with the distance from the impeller, and a sudden reduction near the walls of the tank. When we compare Figs. 9 and 10, we can see that in the latter the magnitude of the velocity vectors is larger, while the low viscosity area for the non-Newtonian fluids becomes greater because of the increased impeller speed.

5. Conclusions and future work

In this study, we evaluated the rheological properties of different mixtures of glycerol and a gel made of polyethylene glycol and Carbomer, which are used in the manufacturing of non-aqueous toothpastes. The constitutive equation that relates the viscosity to the fluid temperature, gel mass fraction and shear rate was well characterized by a power law model. We then developed a CFD model of a simple stirred tank and we implemented the rheology model in it. We validated the model using a sophisticated experimental setup able to accurately measure the power consumption of the impeller, which involves the use of an air bearing and a load cell instead of torque meters. This work will set the ground for the modelling of a real system for the manufacturing of non-aqueous toothpastes.

Acknowledgements

The authors would like to express gratitude to GlaxoSmithKline Consumer Healthcare and to the EPSRC for the financial support given to this project.

References

Adams, L., Barigou, M., 2007. CFD analysis of caverns and pseudo-caverns developed during mixing of non-Newtonian fluids. Chem. Eng. Res. Des. 85, 598–604.

Amanullah, A., Hjorth, S.A., Nienow, A.W., 1997. Cavern sizes generated in highly shear thinning viscous fluids by SCABA 3SHP1 impellers. Food Bioprod. Process. 75, 232–238.

Ameur, H., 2015. Energy efficiency of different impellers in stirred tank reactors. Energy 93, 1980–1988.

Ascanio, G., Castro, B., Galindo, E., 2004. Measurement of power consumption in stirred vessels—a review. Chem. Eng. Res. Des. 82, 1282–1290.

Barry, B., Meyer, M., 1979. The rheological properties of carbopol gels I. Continuous shear and creep properties of carbopol gels. Int. J. Pharm. 2, 1–25.

Bonacucina, G., Martelli, S., Palmieri, G.F., 2004. Rheological, mucoadhesive and release properties of Carbopol gels in hydrophilic cosolvents. Int. J. Pharm. 282, 115–130.

Bulnes-Abundis, D., Alvarez, M.M., 2013. The simplest stirred tank for laminar mixing: mixing in a vessel agitated by an off-centered angled disc. Aiche J. 59, 3092–3108.

Busciglio, A., Montante, G., Paglianti, A., 2015. Flow field and homogenization time assessment in continuously-fed stirred tanks. Chem. Eng. Res. Des. 102, 42–56.

Chapple, D., Kresta, S., Wall, A., Afacan, A., 2002. The effect of impeller and tank geometry on power number for a pitched blade turbine. Chem. Eng. Res. Des. 80, 364–372.

Chhabra, R.P., Richardson, J.F., 2011. Non-Newtonian Flow and Applied Rheology: Engineering Applications. Butterworth-Heinemann.

Coussot, P., Tocquer, L., Lanos, C., Ovarlez, G., 2009. Macroscopic vs. local rheology of yield stress fluids. J. Non-Newton. Fluid Mech. 158, 85–90.

Dyster, K.N., Koutsakos, E., Jaworski, Z., Nienow, A.W., 1993. An Lda study of the radial discharge velocities generated by a rushton turbine—Newtonian fluids: re-greater-than-or-equal-to-5. Chem. Eng. Res. Des. 71, 11–23.

Green, D.W., 2008. Perry's Chemical Engineers' Handbook. McGraw-Hill, New York, pp. 48–49, Section 8.

Hurtado, F.J., Kaiser, A.S., Zamora, B., 2015. Fluid dynamic analysis of a continuous stirred tank reactor for technical optimization of wastewater digestion. Water Res. 71, 282–293.

Islam, M.T., Rodriguez-Hornedo, N., Ciotti, S., Ackermann, C., 2004. Rheological characterization of topical carbomer gels neutralized to different pH. Pharm. Res. 21, 1192–1199.

Kazemzadeh, A., Ein-Mozaffari, F., Lohi, A., Pakzad, L., 2016. Effect of the rheological properties on the mixing of Herschel–Bulkley fluids with coaxial mixers: applications of tomography, CFD, and response surface methodology. Can. J. Chem. Eng. 9999, 1–13.

Khapre, A., Munshi, B., 2015. Numerical investigation of hydrodynamic behavior of shear thinning fluids in stirred tank. J. Taiwan Inst. Chem. Eng. 56, 16–27.

Kim, J.Y., Song, J.Y., Lee, E.J., Park, S.K., 2003. Rheological properties and microstructures of Carbopol gel network system. Colloid Polym. Sci. 281, 614–623.

Kresta, S.M., Etchells III, A.W., Dickey, D.S., Atiemo-Obeng, V.A., 2015. Adv. Ind. Mixing.

Metzner, A., Otto, R., 1957. Agitation of non-Newtonian fluids. AIChE J. 3, 3–10.

Naterer, G.F., Adeyinka, O.B., 2009. Imaging velocimetry measurements for entropy production in a rotational magnetic stirring tank and parallel channel flow. Entropy 11, 334–350.

Nienow, A.W., Edwards, M., Harnby, N., 1997. Mixing in the Process Industries. Butterworth-Heinemann.

Pakzad, L., Ein-Mozaffari, F., Upreti, S.R., Lohi, A., 2013a. Agitation of Herschel–Bulkley fluids with the Scaba-anchor coaxial mixers. Chem. Eng. Res. Des. 91, 761–777.

Pakzad, L., Ein-Mozaffari, F., Upreti, S.R., Lohi, A., 2013b. A novel and energy-efficient coaxial mixer for agitation of non-Newtonian fluids possessing yield stress. Chem. Eng. Sci. 101, 642–654.

Patel, D., Ein-Mozaffari, F., Mehrvar, M., 2012. Improving the dynamic performance of continuous-flow mixing of pseudoplastic fluids possessing yield stress using Maxblend impeller. Chem. Eng. Res. Des. 90, 514–523.

Patel, D., Ein-Mozaffari, F., Mehrvar, M., 2015. Effect of rheological parameters on non-ideal flows in the continuous-flow mixing of biopolymer solutions. Chem. Eng. Res. Des. 100, 126–134.

Paul, E.L., Atiemo-Obeng, V.A., Kresta, S.M., 2004. Handbook of Industrial Mixing: Science and Practice. John Wiley & Sons, Hoboken, NJ.

Ramsay, J., Simmons, M.J.H., Ingram, A., Stitt, E.H., 2016. Mixing of Newtonian and viscoelastic fluids using butterfly impellers. Chem. Eng. Sci. 139, 125–141.

Rieger, F., Novak, V., 1973. Power consumption of agitators in highly viscous non-Newtonian liquids. Trans. Inst. Chem. Eng. 51, 105–111.

Rushton, J., Costich, E., Everett, H., 1950. Power characteristics of mixing impellers. 1. Chem. Eng. Progress 46, 395–404.

Schramm, G., 1994. A Practical Approach to Rheology and Rheometry. Haake Karlsruhe.

Shekhar, S.M., Jayanti, S., 2002. CFD study of power and mixing time for paddle mixing in unbaffled vessels. Chem. Eng. Res. Des. 80, 482–498.
Sossa-Echeverria, J., Taghipour, F., 2014. Effect of mixer geometry and operating conditions on flow mixing of shear thinning fluids with yield stress. Aiche J. 60, 1156–1167.
Sossa-Echeverria, J., Taghipour, F., 2015. Computational simulation of mixing flow of shear thinning non-Newtonian fluids with various impellers in a stirred tank. Chem. Eng. Process.: Process Intensif. 93, 66–78.
Sun, X.S., Sakai, M., 2016. Numerical simulation of two-phase flows in complex geometries by using the volume-of-fluid/immersed-boundary method. Chem. Eng. Sci. 139, 221–240.
Torrez, C., Andre, C., 1999. Simulation of a Rushton turbine mixing yield stress fluids: application of the Metzner–Otto concept. Chem. Eng. Technol. 22, 701–706.
Venneker, B.C.H., Derksen, J.J., Van Den Akker, H.E.A., 2010. Turbulent flow of shear-thinning liquids in stirred tanks—the effects of Reynolds number and flow index. Chem. Eng. Res. Des. 88, 827–843.
Wu, H., Patterson, G.K., 1989. Laser-doppler measurements of turbulent-flow parameters in a stirred mixer. Chem. Eng. Sci. 44, 2207–2221.
Zhang, L.P., Zhang, J., Li, C.H., Bao, J., 2014. Rheological characterization and CFD modeling of corn stover-water mixing system at high solids loading for dilute acid pretreatment. Biochem. Eng. J. 90, 324–332.
Zlokarnik, M., 2003. Stirring. Wiley Online Library.

Appendix A.

In this Appendix we provide the values of the power law model coefficients (Eq. (5)) that can be used to predict the viscosity of mixtures of the Carbomer gel and glycerol for shear rates in the

Table A1 – Values of K [kg $s^{(n-2)}$ m^{-1}] for different temperatures and gel mass fractions.

T (°C)\ gel mass fraction	1	0.9	0.8	0.7	0.6	0.5	0.4	0.3	0.2	0.1	0
25	518.9	499.8	407.2	431.0	284.4	268.45	132.5	69.56	32.77	6.123	1.000
30	360.3	358.4	310.8	317.5	222.3	180.75	102.1	45.88	22.11	3.604	0.600
35	301.2	320.8	275.5	276.1	194.1	156.20	84.99	37.79	17.84	2.834	0.400
40	291.5	287.1	249.6	247.5	172.6	137.82	73.88	32.28	14.85	2.279	0.300
45	266.9	262.9	227.8	225.3	155.8	123.35	65.71	28.21	12.78	1.848	0.200
50	243.6	242.1	209.9	206.0	141.5	111.70	59.11	25.12	11.09	1.519	0.150
55	222.6	220.0	190.3	186.0	128.8	101.90	51.58	22.48	9.732	1.243	0.120
60	200.1	204.2	175.3	171.9	119.0	94.16	45.91	19.98	8.326	0.9898	0.090
65	183.7	188.1	164.1	160.2	110.9	86.38	42.48	18.16	7.446	0.8405	0.070
70	172.2	178.4	154.8	151.0	103.3	81.31	38.77	17.27	7.048	0.7789	0.055
75	157.9	165.2	143.1	141.1	96.27	76.50	33.50	16.28	6.503	0.7199	0.040
80	144.5	153.5	131.5	132.0	91.35	71.79	28.93	15.26	5.889	0.6618	0.033
85	132.0	141.8	119.7	124.0	85.61	67.69	24.62	14.25	5.333	0.6181	0.026

Table A2 – Values of n for different temperatures and gel mass fractions.

T (°C)\ gel mass fraction	1	0.9	0.8	0.7	0.6	0.5	0.4	0.3	0.2	0.1	0
25	0.3781	0.3868	0.3867	0.4112	0.4437	0.4453	0.4923	0.5533	0.6148	0.768	1.000
30	0.3732	0.3826	0.3911	0.4006	0.4342	0.4526	0.4833	0.5714	0.6403	0.8367	1.000
35	0.3663	0.3654	0.3779	0.3918	0.4223	0.4379	0.474	0.5604	0.6307	0.8271	1.000
40	0.3476	0.3574	0.3674	0.3798	0.4089	0.4259	0.4633	0.5493	0.6214	0.8179	1.000
45	0.3342	0.345	0.3551	0.3671	0.3963	0.4141	0.4512	0.5381	0.6096	0.8115	1.000
50	0.3245	0.3321	0.3415	0.3558	0.3845	0.4015	0.4392	0.5262	0.6006	0.805	1.000
55	0.3119	0.3277	0.3375	0.3509	0.3746	0.3883	0.436	0.5171	0.5933	0.8041	1.000
60	0.3266	0.328	0.3393	0.3462	0.3695	0.3843	0.4409	0.5176	0.6072	0.8198	1.000
65	0.3187	0.3229	0.3309	0.3379	0.357	0.3761	0.4273	0.5089	0.598	0.8117	1.000
70	0.2843	0.2859	0.2996	0.3112	0.3362	0.3492	0.402	0.4796	0.5617	0.7829	1.000
75	0.2741	0.2751	0.2898	0.2987	0.3275	0.3359	0.3974	0.4647	0.5495	0.7649	1.000
80	0.263	0.262	0.2818	0.286	0.31	0.3232	0.3937	0.4508	0.541	0.7488	1.000
85	0.2514	0.2504	0.2752	0.2721	0.2992	0.3071	0.3952	0.4396	0.5358	0.7294	1.000

Table A3 – Averaged percentage errors in the estimation of the K and n coefficients to be used in the power law model.

T (°C)\ gel mass fraction	1	0.9	0.8	0.7	0.6	0.5	0.4	0.3	0.2	0.1	0
25	3.2%	4.3%	7.7%	4.8%	9.0%	6.3%	6.9%	6.7%	7.2%	7.5%	0.0%
30	7.7%	7.4%	8.2%	7.2%	8.3%	8.0%	7.0%	6.1%	5.0%	1.0%	0.0%
35	8.3%	8.1%	8.6%	7.0%	7.6%	7.7%	6.7%	5.6%	4.7%	0.9%	0.0%
40	8.1%	8.2%	8.4%	7.0%	7.5%	7.5%	6.5%	5.0%	4.3%	0.8%	0.0%
45	8.6%	8.5%	8.6%	7.2%	7.6%	7.4%	6.7%	4.8%	4.3%	0.8%	0.0%
50	8.9%	9.0%	9.1%	7.5%	7.9%	7.8%	6.8%	4.7%	4.2%	0.7%	0.0%
55	10.2%	9.0%	9.0%	7.6%	8.1%	7.9%	6.5%	4.6%	4.2%	0.6%	0.0%
60	7.2%	7.4%	7.4%	7.1%	7.5%	7.7%	5.7%	4.2%	2.9%	3.5%	0.0%
65	7.2%	7.1%	7.2%	7.0%	8.0%	7.8%	6.1%	4.3%	2.9%	2.7%	0.0%
70	10.4%	10.6%	9.9%	9.2%	9.5%	9.5%	7.6%	6.1%	5.2%	0.4%	0.0%
75	11.1%	11.2%	10.3%	10.0%	9.8%	9.9%	8.1%	6.7%	5.5%	0.7%	0.0%
80	11.7%	12.0%	10.4%	10.7%	10.8%	10.7%	8.4%	7.3%	5.8%	1.1%	0.0%
85	12.5%	12.6%	10.6%	11.6%	11.2%	11.4%	8.2%	7.8%	5.7%	1.7%	0.0%

range of 1–250 s^{-1} and temperatures in the range of 25–85 °C (Tables A1 and A2).

$$\eta = K\dot{\gamma}^{(n-1)} \tag{5}$$

The averaged percentage errors in the estimation of the K and n coefficients to be used in the power law model are presented in Table A3.

Appendix B.

In this Appendix we provide the values of the Herschel–Bulkley model parameters (Eq. (7)) that can be used to predict the viscosity of mixtures of the Carbomer gel and glycerol for shear rates in the range of 1–250 s^{-1} and temperatures in the range of 25–85 °C (Tables B1–B3).

$$\eta = \begin{cases} \infty, & \tau \le \tau_0 \\ \dfrac{\tau_0}{\dot{\gamma}} + K\dot{\gamma}^{(n-1)}, & \tau \ge \tau_0 \end{cases} \tag{7}$$

Table B1 – Values of τ_0 [Pa] for different temperatures and gel mass fractions for the Herschel–Bulkley model.

T (°C)\ gel mass fraction	1	0.9	0.8	0.7	0.6	0.5	0.4	0.3	0.2	0.1	0
25	39.24	38.00	39.24	37.78	30.66	27.78	15.27	9.232	0	0	0
30	34.17	34.14	30.72	30.55	23.63	20.34	11.78	6.062	0	0	0
35	29.46	29.91	27.00	25.70	19.63	16.62	9.459	4.757	0	0	0
40	26.30	26.55	23.62	22.64	16.87	14.25	7.949	3.853	0	0	0
45	21.83	23.96	21.38	20.31	15.25	12.43	6.989	3.285	0	0	0
50	21.51	22.02	19.61	18.44	13.42	11.16	6.154	2.858	0	0	0
55	19.86	19.37	17.01	16.38	12.43	10.14	5.276	2.515	0	0	0
60	14.76	15.30	13.44	13.39	10.08	8.160	4.143	1.509	0	0	0
65	13.45	13.91	12.18	12.30	9.424	7.446	3.774	1.644	0	0	0
70	14.71	15.49	13.42	13.11	9.406	7.804	3.845	1.913	0	0	0
75	13.50	14.44	12.28	12.27	8.902	7.267	3.380	1.798	0	0	0
80	12.35	13.40	11.06	11.53	8.401	6.774	2.912	1.680	0	0	0
85	11.35	17.94	9.939	10.88	7.707	6.427	2.462	1.552	0	0	0

Table B2 – Values of K [kg $s(n^{-2})$ m^{-1}] for different temperatures and gel mass fractions for the Herschel–Bulkley model.

T (°C)\ gel mass fraction	1	0.9	0.8	0.7	0.6	0.5	0.4	0.3	0.2	0.1	0
25	480.9	463.0	370.6	395.4	263.0	243.1	118.9	61.66	32.77	6.123	1.000
30	328.4	326.5	282.3	289.1	199.9	162.4	91.56	40.70	22.11	3.604	0.600
35	294.2	292.7	250.4	252.0	175.9	141.1	76.49	33.67	17.84	2.834	0.400
40	266.7	262.2	227.4	226.2	156.1	124.8	66.68	28.89	14.85	2.279	0.300
45	245.2	240.3	207.7	206.1	141.8	111.9	59.35	25.31	12.78	1.848	0.200
50	223.2	221.3	191.5	188.6	129.2	101.4	53.49	22.58	11.09	1.519	0.150
55	203.8	201.6	174.2	170.5	118.0	92.50	46.75	20.23	9.732	1.24	0.120
60	185.7	189.4	162.3	159.0	110.5	86.45	42.02	18.58	8.326	0.9898	0.090
65	170.6	174.6	152.3	148.4	103.3	79.33	38.94	16.63	7.446	0.8405	0.070
70	158.1	163.6	142.0	138.5	95.68	74.00	35.21	15.55	7.048	0.7789	0.055
75	145.0	151.4	131.4	129.4	90.10	69.67	30.38	14.66	6.503	0.7199	0.040
80	132.7	140.6	120.9	121.0	85.05	65.41	26.24	13.74	5.889	0.6618	0.033
85	121.1	125.0	110.2	113.6	79.75	61.62	22.34	12.84	5.333	0.6181	0.026

Table B3 – Values of n for different temperatures and gel mass fractions for the Herschel–Bulkley model.

T (°C)\ gel mass fraction	1	0.9	0.8	0.7	0.6	0.5	0.4	0.3	0.2	0.1	0
25	0.3970	0.4061	0.4060	0.4318	0.4463	0.4670	0.5170	0.5810	0.6148	0.7680	1
30	0.3919	0.4018	0.4106	0.4206	0.4483	0.4752	0.5074	0.6000	0.6403	0.8367	1
35	0.3786	0.3837	0.3968	0.4114	0.4334	0.4598	0.4977	0.5884	0.6307	0.8271	1
40	0.3650	0.3753	0.3858	0.3987	0.4233	0.4472	0.4865	0.5768	0.6214	0.8179	1
45	0.3509	0.3623	0.3728	0.3855	0.4090	0.4348	0.4738	0.5650	0.6096	0.8115	1
50	0.3407	0.3487	0.3585	0.3735	0.4019	0.4216	0.4612	0.5525	0.6006	0.8050	1
55	0.3275	0.3441	0.3543	0.3684	0.3905	0.4077	0.4578	0.5429	0.5933	0.8041	1
60	0.3429	0.3444	0.3563	0.3635	0.3885	0.4035	0.4629	0.5378	0.6072	0.8198	1
65	0.3346	0.3390	0.3474	0.3548	0.3791	0.3949	0.4486	0.5333	0.5980	0.8117	1
70	0.2985	0.3002	0.3145	0.3268	0.3580	0.3666	0.4221	0.5036	0.5617	0.7829	1
75	0.2878	0.2888	0.3043	0.3136	0.3455	0.3527	0.4173	0.4879	0.5495	0.7649	1
80	0.2762	0.2751	0.2959	0.3003	0.3313	0.3394	0.4134	0.4733	0.5410	0.7488	1
85	0.2640	0.2630	0.2890	0.2857	0.3228	0.3225	0.4150	0.4616	0.5358	0.7294	1